

Ultra-High Energy Cosmic Ray Probes of Large Scale Structure and Magnetic Fields*

Günter Sigl^{a,b}, Francesco Miniati^c, Torsten A. Enßlin^c

^a *GReCO, Institut d'Astrophysique de Paris, C.N.R.S., 98 bis boulevard Arago, F-75014 Paris, France*

^b *Fédération de Recherche Astroparticule et Cosmologie,
Université Paris 7, 2 place Jussieu, 75251 Paris Cedex 05, France*

^c *Max-Planck Institut für Astrophysik, Karl-Schwarzschild-Str. 1, 85741 Garching, Germany*

We study signatures of a structured universe in the multi-pole moments, auto-correlation function, and cluster statistics of ultra-high energy cosmic rays above 10^{19} eV. We compare scenarios where the sources are distributed homogeneously or according to the baryon density distribution obtained from a cosmological large scale structure simulation. The influence of extragalactic magnetic fields is studied by comparing the case of negligible fields with fields expected to be produced along large scale shocks with a maximal strength consistent with observations. We confirm that strongly magnetized observers would predict considerable anisotropy on large scales, which is already in conflict with current data. In the best fit scenario only the sources are strongly magnetized, although deflection can still be considerable, of order 20° up to 10^{20} eV, and a pronounced GZK cutoff is predicted. We then discuss signatures for future large scale full-sky detectors such as the Pierre Auger and EUSO projects. Auto-correlations are sensitive to the source density only if magnetic fields do not significantly affect propagation. In contrast, for a weakly magnetized observer, degree scale auto-correlations below a certain level indicate magnetized discrete sources. It may be difficult even for next generation experiments to distinguish between structured and unstructured source distributions.

PACS numbers: 98.70.Sa, 13.85.Tp, 98.65.Dx, 98.54.Cm

I. INTRODUCTION

The origin of ultra-high energy cosmic rays (UHECRs) is still one of the most challenging problems of modern astrophysics. It is an open question which mechanism is responsible for producing particles up to 10^{20} eV and beyond and where the corresponding sources can be found [1, 2]. Although statistically meaningful information about the UHECR energy spectrum and arrival direction distribution has been accumulated, no conclusive picture for the nature and distribution of the sources emerges naturally from the data (for a short overview on the relevant literature see Ref. [3]). There is on the one hand the approximate isotropic arrival direction distribution [4] which indicates that we are observing a large number of weak or distant sources. On the other hand, there are also indications which point more towards a small number of local and therefore bright sources: First, there seem to be statistically significant multi-plets of events from the same directions within a few degrees [4, 5]. Second, nucleons above $\simeq 70$ EeV suffer heavy energy losses due to photo-pion production on the cosmic microwave background — the Greisen-Zatsepin-Kuzmin (GZK) effect [6] — which limits the distance to possible sources to less than $\simeq 100$ Mpc [7]. For a uniform source distribution this would predict a “GZK cutoff”, a drop in the spectrum. However, the existence of this “cutoff” is not established yet from the observations [8]. In fact, whereas a cut-off seems con-

sistent with the few events above 10^{20} eV recorded by the fluorescence detector HiRes [9], it is not compatible with the 11 events (also above 10^{20} eV) measured by the AGASA ground array [10]. The solution of this problem may have to await the completion of the Pierre Auger project [11] which will combine the two complementary detection techniques adopted by the aforementioned experiments.

Such apparently contradicting hints could easily be solved if it would be possible to follow the UHECR trajectories backwards to their sources. However, this may be complicated by the possible presence of extragalactic magnetic fields, which would deflect the particles during their travel. Furthermore, since the GZK-energy losses are of stochastic nature, even a detailed knowledge of the extragalactic magnetic fields would not necessarily allow to follow a UHECR trajectory backwards to its source since the energy and therefore the Larmor radius of the particles have changed in an unknown way. Therefore it is not clear if charged particle astronomy with UHECRs is possible in principle or not. And even if possible, it remains unclear to which degree the angular resolution would be limited by magnetic deflection.

Quite a few simulations of the effect of extragalactic magnetic fields (EGMF) on UHECRs exist in the literature, but usually idealizing assumptions concerning properties and distributions of sources or EGMF or both are made: In Refs. [12, 13, 14, 15, 16] sources and EGMF follow a pancake profile mimicking the local supergalactic plane. In Ref. [17] highly structured EGMF have been obtained from constrained simulations, but the source distribution has been assumed homogeneous. In other studies EGMF have been approximated in a number of fashions: as negligible [18, 19], as uniform [20], or as

*version published as Phys. Rev. D 70, 043007 (2004), Copyright The American Physical Society 2004.

organized in spatial cells with a given coherence length and a strength depending as a power law on the local density [21].

However, the presence of the above mentioned *apparently contradicting hints* indicate that the existing data set might already carry information on non-trivial properties of sources and EGMF. Here, we want to address the following questions relevant to charged particle astronomy:

1. Do we observe a large number of dim or a small number of bright UHECR sources?
2. Is the source location distribution statistically homogeneous, or does it follow the matter distribution in the local Universe?
3. Are the particles strongly deflected by intergalactic magnetic fields?
4. What are the magnetic fields surrounding sources and observer ?
5. Can we discriminate between the case of sources with practical identical luminosities and the case of a power-law luminosity distribution?

The means by which we want to study these questions are comparisons of simulated datasets to the observed one by statistical tests on the arrival direction multi-pole moment and auto-correlation distributions, on the multiplet statistics, and on the UHECR energy spectrum. The simulated UHECR events are produced by following the trajectories of particles through a large-scale structure simulation which included a numerical model for the generation and evolution of the EGMF. We thereby extend our former studies [3, 22] to a larger parameter space and a higher degree of realism.

The most important results of these former studies are: A local component of sources within $\lesssim 100$ Mpc alone cannot explain satisfactorily the observed isotropy at energies $\lesssim 4 \times 10^{19}$ eV [3]. In Ref. [22] and the present study we therefore take into account sources at cosmological distances by periodically repeating the large scale structure simulation box. As a result we found that in combination, a comparison of spherical multi-poles for $l \leq 10$ and of the auto-correlation at angles $\theta \lesssim 20^\circ$ between observed and simulated data moderately favors a scenario in which (i) UHECR sources have a density $n_s \sim 10^{-5} \text{ Mpc}^{-3}$ and follow the matter distribution (ii) magnetic fields are relatively pervasive within the large scale structure, including filaments, and with a strength of order of a μG in galaxy clusters (iii) the local extragalactic environment is characterized by a weak magnetic field below $0.1 \mu\text{G}$. This is in contrast to Ref. [3] where the neglect of cosmological sources marginally favored observers immersed in $\sim 0.1 \mu\text{G}$ fields. Finally, we found that the degree-scale auto-correlation functions above $\simeq 4 \times 10^{19}$ eV can serve as a discriminator between magnetized and unmagnetized sources.

In the present paper we specifically focus on signatures for the structure, density and luminosity distribution of UHECR sources, as well as for magnetic fields surrounding sources and observer. We will find, as expected, that for most of these observables, the current data set does not allow to clearly distinguish between limiting cases. We will therefore discuss how future experiments such as the Pierre Auger [11] and EUSO [23] projects will improve the prospects to measure these observables.

Here, we restrict ourselves to UHECR nucleons, and we neglect the Galactic contribution to the deflection of UHECR since typical proton deflection angles in galactic magnetic fields of several μG are $\lesssim 10^\circ$ above 4×10^{19} eV [24], and thus in general are small compared to extragalactic deflection in the scenarios studied in the present paper.

The simulations are described in more detail in the next section. There we also describe the general features of our method and define the statistical quantities used for comparison with the data. Sect. 3 presents how large scale multi-poles and small-scale auto-correlations probe magnetization and UHECR source characteristics. It constitutes the main part of the present paper. We conclude in Sect. 4.

II. OUTLINE OF THE NUMERICAL TECHNIQUE

In the next section we will investigate, from a statistical point of view as defined below, the viability of various scenarios for the propagation of UHECRs in an extragalactic environment. These scenarios are listed in Tab. I and differ in the UHECR source distributions, the strength of the EGMF, and the location of an hypothetical observer on Earth. The latter will also lead to different strengths of the EGMF within a few Mpc from the observer. In the following sections we describe in detail how the various scenarios are characterized.

A. Large Scale Structure and Extragalactic Magnetic Fields

The magnetized extragalactic environment which we use for our experiments is produced by a simulation of the large scale structure of the Universe. The simulation was carried out within a computational box of $50 h^{-1} \text{ Mpc}$ length on a side, with normalized Hubble constant $h \equiv H_0 / (100 \text{ km s}^{-1} \text{ Mpc}^{-1}) = 0.67$, and using a comoving grid of 512^3 zones and 256^3 dark matter particles. This is the same large scale structure simulation that was used in Refs. [3, 22] and is further described in [25].

The EGMF adopted here is based on the numerical model developed in [26] which has been shown to be compatible with existing Faraday rotation measures with lines of sight both through clusters and the diffuse intergalactic medium. Thus, at simulation start the EGMF

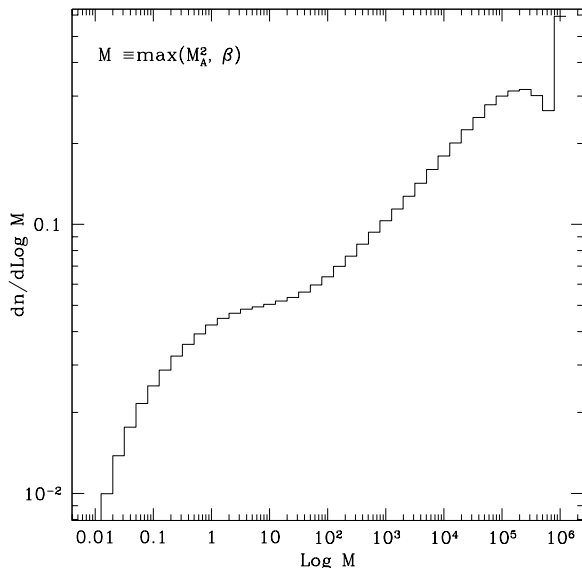


FIG. 1: Distribution of the number of cells n as a function of the maximum M of the Alfvén Mach number and the plasma beta parameter.

was initialized to zero and subsequently its seeds were generated at cosmic shocks through the Biermann battery mechanism [27]. This approach is alternative to the case in which the initial magnetic field is set uniform over the whole simulated volume. Since cosmic shocks form primarily around collapsing structures including filaments, the above approach avoids generating EGMF in cosmic voids. An alternative, more realistic but also much more complicated scenario is discussed in Ref. [28], in which magnetic fields are injected into the intergalactic medium by galactic outflows. Whichever the mechanism that generates it, the magnetic field is then evolved according to the induction equation and is therefore amplified in different parts of the universe by shear flows and compression according to the velocity field provided by the simulated gas component.

As already pointed out in Ref. [3], given the tiny values of the initial seeds generated through the Biermann mechanism, the field strength at simulation end (when the cosmological redshift equals zero) is much smaller than what is observed in galaxy clusters via a number of experiments [29]. Therefore, in order to avoid such discrepancies, it is necessary to change the normalization of the simulated magnetic field strength. Our renormalization procedure simply involves a rescaling of the overall magnetic field in the computational box, such that the magnetic field in the core region of a Coma-like galaxy cluster is *predicted* to be of order of a μG or so, as indicated by Faraday rotation measures [29]. As a result of this rescaling, the magnetic field strength volume averaged over $\simeq 0.5\text{Mpc}$ within typical cluster cores is between 0.7 and 2.5 μG . Since the magnetic field strength,

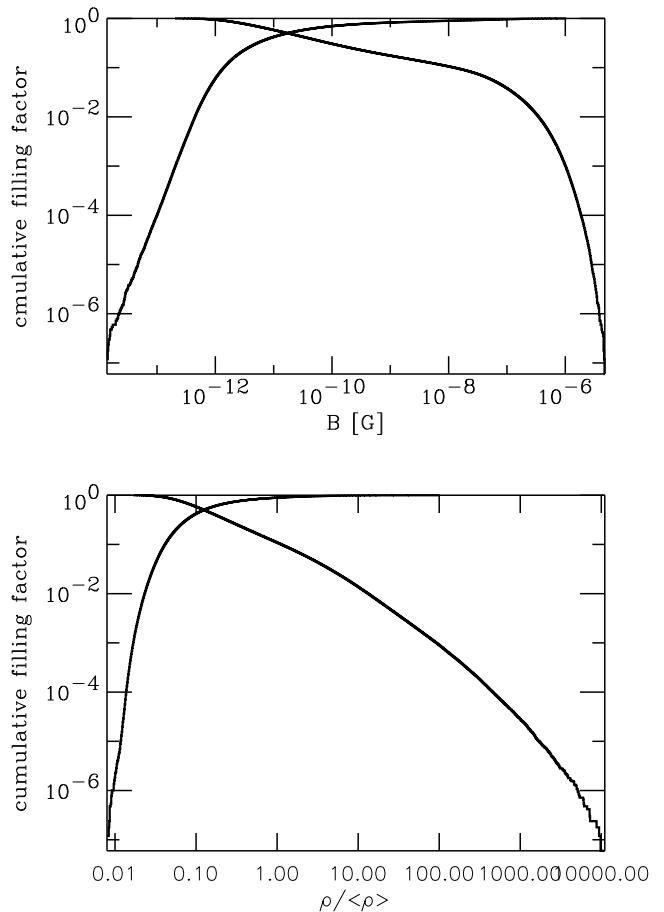


FIG. 2: The cumulative filling factors for EGMF strength, (middle panel) baryon density (lower panel, in units of average baryon density) above (decreasing curves) and below (increasing curves) a given threshold, as a function of that threshold.

B , in collapsed structures follows a well defined scaling relation with the structures virial temperature [30], the renormalization of the magnetic field as described above can be easily carried out even though Coma like galaxy clusters do not form in our simulation due to the relatively small computational box.

Lacking direct measurements of magnetic fields in filaments, we assume that the topology and relative strength of the large scale intergalactic magnetic field in different parts of the Universe is as reproduced by our numerical simulation. However, as already pointed out the resulting EGMF is consistent with statistics of existing Faraday rotation measures with line of sight through filaments despite the fact that the magnetic field strength can be close to the equipartition value with the gas total energy [26].

It is worth pointing out that, because of the very scarce observational constraints on intergalactic magnetic fields, both our assumptions have limitations. For example, an independent experiment based on the detection from the

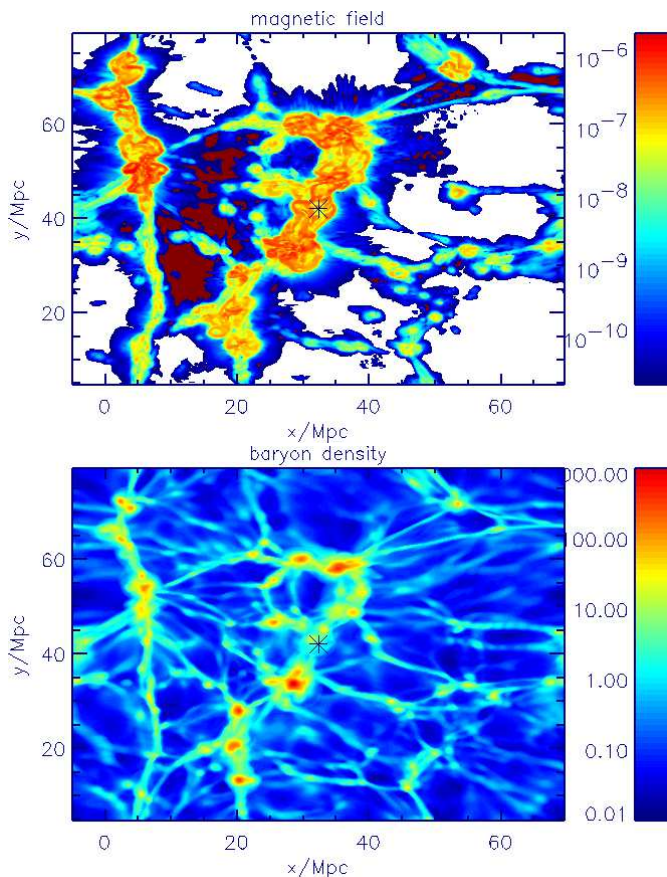


FIG. 3: Log-scale two-dimensional cut through magnetic field total strength in Gauss (color scale in Gauss, upper panel) and baryon density in units of average baryon density (color scale, lower panel). The observer is in the center of the figures and is marked by a star. The EGMF strength at the observer is $\simeq 0.1 \mu\text{G}$. Note that both panels correspond to the same cuts through the full large scale simulation box.

Coma cluster of radio synchrotron emission and hard X-rays interpreted as inverse Compton emission, would suggest that magnetic fields in this cluster are lower by about an order of magnitude compared to what we are assuming [31]. Similarly, and more importantly, one cannot exclude the possibility of much smaller magnetic fields in filaments than we assume, although some evidence for magnetic fields in filaments at the level of a tenth of a μG may already exist [32].

According to our simulation scenario and with the assumptions made, we find that EGMF are significant only within filaments and groups/clusters of galaxies. In Fig. 1 we test the assumption that the magnetic field is passive. In order for the magnetic field to be dynamically important both the Alfvénic Mach number, $M_A = v/v_A = v/B/(4\pi\rho)^{1/2}$, and the plasma β parameter, $\beta = P_{gas}/(B^2/8\pi)$ must be smaller than unity. Thus in Fig. 1 we plot a histogram of the fraction of cells as a function of $M = \max(M_A^2, \beta)$. The histogram shows that the condition of dynamically unimportant magnetic field

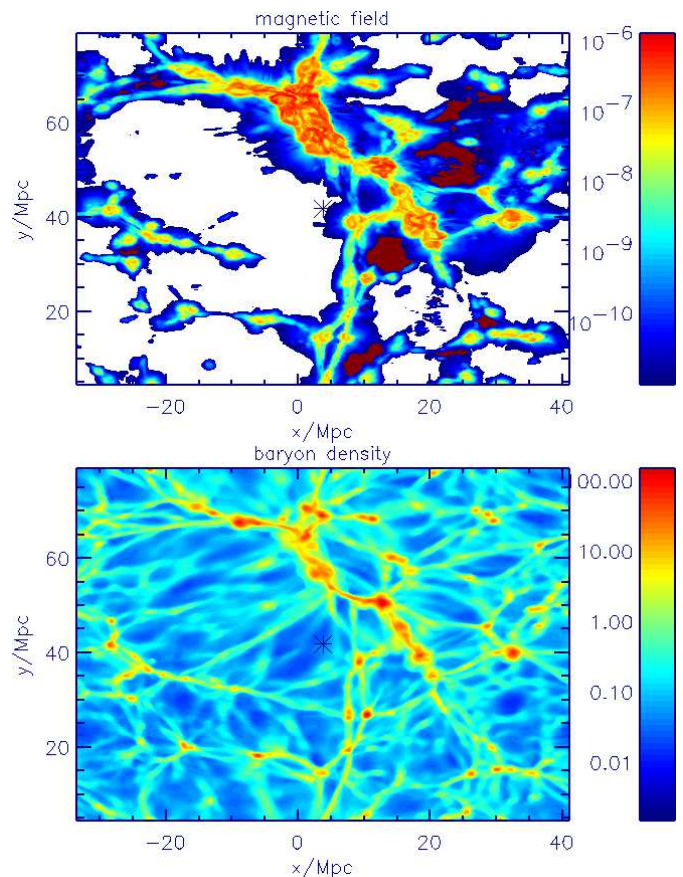


FIG. 4: Same as Fig. 3, but for an observer situated in a small void where the EGMF strength is $\simeq 10^{-11} \text{G}$.

is violated only in a very small fraction of the volume, which does not affect the evolution of the simulation in any significant way. Furthermore, only a fraction of the cells in those bins is characterized by a magnetic field capable of affecting the trajectory of UHECRs. In any case, as discussed in Sec. IV we consider the case of a field strength normalization reduced by a factor 10 with respect to our fiducial model. This would correspond to a left-shift of the x-axis in Fig. 1 of two decades, such that the EGMF is virtually dynamically unimportant in all cells of the simulation.

About 90 percent of the volume is filled with fields $\lesssim 10 \text{nG}$ and in the voids fields are $\lesssim 10^{-11} \text{G}$. In Fig. 2 we show the cumulative filling factors for both the EGMF strength and the baryonic gas. The volume field averages are $\langle |B| \rangle \simeq 1.5 \times 10^{-8} \text{G}$, and $\langle \langle B^2 \rangle \rangle^{1/2} \simeq 7.9 \times 10^{-8} \text{G}$, with coherence lengths $\lesssim \text{Mpc}$ in the strong field regions, and thus compatible with Faraday rotation bounds [26, 29]. Note that the hallmark of a highly structured field is a ratio $\langle \langle B^2 \rangle \rangle^{1/2} / \langle |B| \rangle \gg 1$, as in the present case.

As in Refs. [3, 22], we explore the case of two observers located at different positions within the simulated volume: The first is located in a filament-like structure with EGMF $\sim 0.1 \mu\text{G}$, and the second at the border of a small

void with EGMF $\sim 10^{-11}$ G. Figs. 3 and 4 show two-dimensional cuts through the EGMF and baryon density around these two observer positions. Notice that the structure of the magnetic field is quite more extended than that for the baryonic gas. Thus a UHECR produced by a source where matter density is high will be subject to the action of magnetic fields within an extended volume surrounding the source, before breaking into a void where magnetic fields are much weaker. A relatively large structure about 17 Mpc away from the weak field observer is identified for calculation purposes as the Virgo cluster. We orient our terrestrial coordinate system so that this cluster is close to the equatorial plane.

B. UHECR Sources

For a given number density of UHECR sources, n_s , we explore both the case in which their spatial distribution is either proportional to the local baryon density, as in Ref. [3], or completely homogeneous. Further, due to the unknown source positions and properties, there will be a cosmic variance in the results. In order to be conservative and maximize this variance, we will therefore assume that all UHECR sources, are distributed in luminosity, Q_i , so that their contribution of UHECR per $\log Q_i$ is roughly constant with Q_i . In addition we allow the spectral index α_i of the emitted power-law distributions of UHECRs to vary and assume that each source accelerates UHECRs up to 10^{21} eV. Specifically, our assumption can be summarized as follows,

$$\begin{aligned} \frac{dn_s}{dQ_i} &\propto Q_i^{-2.2} \quad \text{for } 1 \leq Q_i \leq Q_{\max} \\ \frac{dn_s}{d\alpha_i} &= \text{const} \quad \text{for } \alpha - \Delta\alpha \leq \alpha_i \leq \alpha + \Delta\alpha \\ E_{\max} &= 10^{21} \text{ eV}, \end{aligned} \quad (1)$$

where Q_i has been put in dimensionless units. The power law distribution in Q_i could be further motivated by the luminosity function of the EGRET γ -ray blazars which has this shape in the power range $10^{46} \text{ erg s}^{-1} \lesssim Q_i \lesssim 10^{48} \text{ erg s}^{-1}$ [33]. Constant source characteristics correspond to $Q_{\max} = 1$, $\Delta\alpha = 0$ in Eq. (1). If not explicitly stated that sources with identical properties are assumed, we will always use $Q_{\max} = 100$, $\Delta\alpha = 0.1$. Finally, the actual value of α , representing the central value of the power law index distribution, together with the total power of injected UHECRs are left as free parameters to be obtained from a best fit analysis when the simulation results are compared with observational data.

We also assume that neither total power, Q_i , nor the power law spectral index, α_i , change significantly on the time scale of UHECR propagation. For energies higher than the GZK cutoff this is not an issue because the sources are nearby and the propagation time, given by the distance in light years added by the time delay provided in Fig. 5, is less than the typical duty cycle of, say,

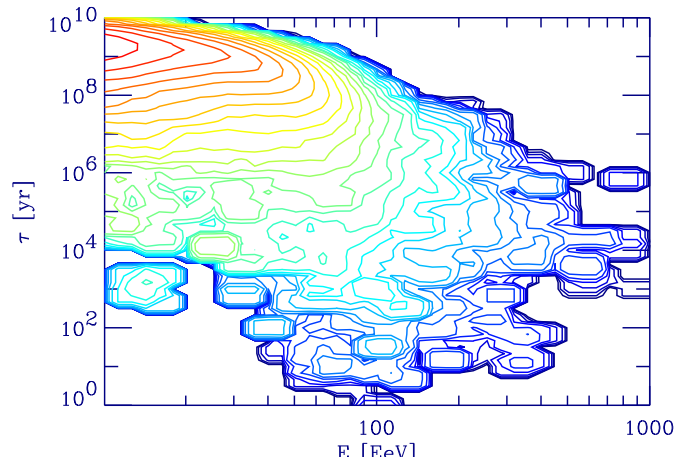


FIG. 5: The distribution of UHECR detection energy E and delay time τ with respect to straight line propagation, for scenario 6 in Tab. I, averaged over 26 realizations of 10^4 simulated trajectories above 10^{19} eV each.

a radio source. On the other hand, for UHECRs of lower energies the propagation time can be up to a few Gyr, see Fig. 5. However, the flux of UHECRs at these energies is dominated by many sources at relatively large distances and, therefore, should not be sensitive to time variations of individual sources.

Taking advantage of the periodic boundary conditions, we build a “hyper volume” by adding periodic images of the simulation box until the linear size of the enclosed volume is $\sim 1.5h^{-1}$ Gpc, that is larger than the energy loss length of nucleons above 10^{19} eV. The distributions of sources and the EGMF are identical in each box for a given realization. Further, in each replicated box within the central Gpc of the hyper volume we place an observer at the same position (relative to the box). This ensures that each observer is still surrounded by several 100 Mpc of sources in each direction. Since the energy loss length for nucleons is $\lesssim 1$ Gpc above 10^{19} eV [34], all relevant distant sources are taken into account in this manner.

C. UHECR Propagation and Event Detection

For each configuration, consisting of a choice of source positions and a set of parameters Q_i and α_i , many nucleon trajectories originating from sources in the Gpc^3 volume were computed numerically. As in previous work [3, 12, 13, 14, 16], particles are propagated taking into account Lorentz forces due to the EGMF and energy losses. In this respect, pion production is treated stochastically, whereas pair production is treated as a continuous energy loss process. Cosmological redshift cannot be taken into account because the propagation time is not known before hand. However, this is a minor effect since the travel time of the trajectories does not exceed ~ 3 Gyr, corresponding to $z \sim 0.6$ down to 10^{19} eV, see Fig. 5.

Trajectories connecting sources and observers in different copies of the simulation box are taken into account.

An *event* was registered and its arrival direction and energy recorded each time the trajectory of the propagating particle crossed a sphere of radius 1.5 Mpc around one of the observers. Events at replicated observers in different boxes are recorded by the same counter. The counter is stopped when 10^4 events (a realization) have been recorded. For more details on this method see Refs. [12, 13, 14]. Modeling the observer as a sphere corresponds to an average over observers located on that sphere. The concrete directions of features in the UHECR sky distribution can never be accurately reconstructed in this approach. However, quantities which only depend on angular distances such as the multi-poles, the auto-correlation function, and the number of event clusters can properly be accounted for by this approach.

Having provided all the relevant definitions, for various scenarios explored in the next section we build statistical samples in the following way. We generate ten realizations for the source positions. For each one of them we use the distributions in Eq. (1), with $Q_{\max} = 100$, $\Delta\alpha = 0.1$, and typically generate 50 realizations with different power Q_i and injection spectral index α_i , whereas the maximal acceleration energy is held constant at 10^{21} eV for simplicity. Thus, for each scenario typically 500 realizations corresponding to different configurations of source positions and emission characteristics are simulated. The variation of results with these configurations constitutes cosmic variance.

D. Data Processing

The process of converting the simulated events to quantities that can be compared with observations was described at length in Ref. [3]. Here we simply summarize the procedure.

For each realization discussed above, the events were used to construct arrival direction probability distributions above a given energy on regular grids of solid angle bins of size $\Delta\theta$ in both declination and right ascension. For the full sky, for example, there are $\simeq 180^\circ/\Delta\theta$ bins in declination and, at declination δ , $\simeq (360^\circ/\Delta\theta)\cos\delta$ bins in right ascension. We chose $\Delta\theta$ small compared to the instrumental angular resolution; typically $\Delta\theta = 0.5^\circ$. The sky distributions are multiplied with the solid-angle dependent exposure function for the respective experiment and are convolved with the angular resolution which is $\simeq 1.6^\circ$ above 4×10^{19} eV and $\simeq 2.5^\circ$ above 10^{19} eV for the AGASA experiment [10]. Due to the poorer angular resolution of the SUGAR data [35], we will use a resolution of 2.5° when combining AGASA and SUGAR data. Energy resolution effects, supposed to be of order $\Delta E/E \simeq 30\%$, are also taken into account.

For the exposure function $\omega(\delta)$ we use the parameterization of Ref. [18] which depends only on declination

δ ,

$$\begin{aligned} \omega(\delta) &\propto \cos(a_0)\cos(\delta)\sin(\alpha_m) + \alpha_m\sin(a_0)\sin(\delta), \\ \text{where } \alpha_m &= \begin{cases} 0 & \text{if } \xi > 1 \\ \pi & \text{if } \xi < -1 \\ \cos^{-1}(\xi) & \text{otherwise} \end{cases}, \quad (2) \\ \text{with } \xi &\equiv \frac{\cos(\theta_m) - \sin(a_0)\sin(\delta)}{\cos(a_0)\cos(\delta)}. \end{aligned}$$

For the AGASA experiment [10] $a_0 = 35^\circ$, $\theta_m = 60^\circ$, and for the former SUGAR experiment [35] on the southern hemisphere $a_0 = -30.5^\circ$, $\theta_m = 55^\circ$. For a full-sky Pierre Auger type experiment we add the exposures for the Southern Auger site with $a_0 = -35^\circ$ and a putative similar Northern site with $a_0 = 39^\circ$, and $\theta_m = 60^\circ$ in both cases, with an assumed angular resolution of $\simeq 1^\circ$.

From the distributions obtained in this way typically 200 mock data sets consisting of N_{obs} observed events were selected randomly. For each such mock data set or for the real data set we then obtained estimators for the spherical harmonic coefficients $C(l)$, the auto-correlation function $N(\theta)$, and the number of multi-plets $M(n)$ of n events within an angle θ_m . As in Refs. [3, 22] the estimator for $C(l)$ is defined as

$$C(l) = \frac{1}{2l+1} \frac{1}{\mathcal{N}^2} \sum_{m=-l}^l \left(\sum_{i=1}^{N_{\text{obs}}} \frac{1}{\omega_i} Y_{lm}(u^i) \right)^2, \quad (3)$$

where ω_i is the total experimental exposure at arrival direction u^i , $\mathcal{N} = \sum_{i=1}^{N_{\text{obs}}} 1/\omega_i$ is the sum of the weights $1/\omega_i$, and $Y_{lm}(u^i)$ is the real-valued spherical harmonics function taken at direction u^i . Also as in Refs. [3, 22] the estimator for $N(\theta)$ is defined as

$$N(\theta) = \frac{C}{S(\theta)} \sum_{j \neq i} \begin{cases} 1 & \text{if } \theta_{ij} \text{ is in same bin as } \theta \\ 0 & \text{otherwise} \end{cases}, \quad (4)$$

and $S(\theta)$ is the solid angle size of the corresponding bin. In Eq. (4) the normalization factor $C = \Omega_e / (N_{\text{obs}}(N_{\text{obs}} - 1))$, with Ω_e denoting the solid angle of the sky region where the experiment has non-vanishing exposure, is chosen such that an isotropic distribution corresponds to $N(\theta) = 1$.

Finally, the multi-plets are obtained as follows: For a given set of N_{obs} ordered events, the first event is considered as a singlet. Then for all other events we check if they lie within distance θ_m of one of the other events defining the center of a multi-plet. If yes, the multiplicity of that multi-plet is increased by one, if not, the event is defined as the center of a new multi-plet, starting as a singlet.

In passing we note that other statistical quantities have been considered in the literature, such as cumulative distributions in right ascension and declination in the context of the Kolmogorov-Smirnov test [36], and the ‘‘information-dimension’’ of the sky distribution [37]. We will not use these statistics in the present work.

The different mock data sets in the various realizations yield the statistical distributions of $C(l)$, $N(\theta)$, and $M(n)$. One defines the average over all mock data sets and realizations as well as two errors. The smaller error (shown to the left of the average in the figures below) is the statistical error, i.e. the fluctuations due to the finite number N_{obs} of observed events, averaged over all realizations. The larger error (shown to the right of the average in the figures below) is the “total error”, i.e. the statistical error plus the cosmic variance. Thus, the latter includes the fluctuations due to finite number of events and the variation between different realizations of observer and source positions.

Given a set of observed and simulated events, after extracting some useful statistical quantities S_i , namely C_l , $N(\theta)$, and $M(n)$ defined above, we define

$$\chi_n \equiv \sum_i \left(\frac{S_{i,\text{data}} - \bar{S}_{i,\text{simu}}}{\Delta S_{i,\text{simu}}} \right)^n \quad (5)$$

where the index i runs over multi-pole l , angular bin of θ , and multiplicity n , respectively. Here, $S_{i,\text{data}}$ refers to S_i obtained from either the real data set or the simulated mock data sets, and $\bar{S}_{i,\text{simu}}$ and $\Delta S_{i,\text{simu}}$ are the average and standard deviations of the simulated data sets. Thus, there is a χ_n for the real data, and a χ_n for each of the simulated mock data sets which consist of the same total number of UHECR events. This measure of deviation from the average prediction can then be used to obtain an overall likelihood for the consistency of a given theoretical model with an observed data set by counting the fraction of simulated data sets with χ_n larger than the one for the real data.

III. RESULTS: PROBING EGMF AND UHECR SOURCE CHARACTERISTICS

We now turn to a systematic discussion of signatures of magnetization and UHECR source characteristics in the angular power spectrum, the auto-correlation function, and the clustering of the UHECR arrival distributions.

The scenarios studied are presented in Tab. I together with a statistical measure of their likelihoods. To summarize, UHECR sources whose number density is given in column 2 are distributed either proportionally to the simulated baryonic density or homogeneously (“yes” or “no”, respectively, in column 3). The observer is either in a region with or without appreciable magnetic fields, as quantified more precisely in Fig. 3 and 4, respectively. Finally, the EGMF is either taken from the simulation with local value as indicated in column 5, or completely neglected (“no EGMF”). For all scenarios our statistical assessments are based on typically 200 simulated mock data sets each for 500 different realizations of source locations and emission characteristics, as discussed in Sects. II.C and II.D above. Scenarios 1-6 in Tab. I have already been presented in Ref. [22], whereas scenarios 7-10 are new.

Columns 7-14 of Tab. I show the likelihood significances discussed in the previous section obtained by comparing the predictions from each scenario with currently available experimental data. Particularly, as in previous studies, we carry out a comparison in terms of multi-poles, auto-correlations and multi-plet statistics. As for the experimental data we use the 57 AGASA+Akeno events above 4×10^{19} eV, when studying the auto-correlation function and clustering properties of UHECRs which are sensitive to small scales. For the large scale multi-poles, however, larger sky coverage including the Southern hemisphere is desirable in order to get realistic estimates of the true multi-poles. Therefore, following Ref. [38], when comparing with multi-poles $l \leq 10$ we will also use the combination of 50 events observed by AGASA (excluding 7 events observed by Akeno) and 49 events seen by SUGAR for a total of 99 events above 4×10^{19} eV. In fact, as pointed out by the authors of Ref. [38], the AGASA and SUGAR experiments have comparable exposure in the northern and southern hemisphere, respectively. In addition, while SUGAR’s angular resolution is much worse than for AGASA and in general prevents a combination of the two data sets, this does not affect multi-poles $l \leq 10$ because they are not sensitive to scales $\lesssim 10^\circ$. Comparing columns 7 with 10 and 8 with 11 in Tab. I shows that the inclusion of SUGAR data does not significantly change the likelihood ranking of simulated scenarios in terms of multi-poles.

Finally, using the combined exposure of AGASA+SUGAR, for each scenario we compute the expected values of the multi-pole coefficient for the $\simeq 1500$ events observed above 10^{19} eV. This is interesting because no sign of anisotropy was found by either the AGASA or the SUGAR experiment at these energies. Since data down to 10^{19} eV are not publicly available, we simply compare our results with a completely isotropic distribution. The corresponding likelihoods are also summarized in Tab. I.

As discussed in Ref. [22], the current best fit is provided by scenario 6, i.e. for structured sources of density $n_s \sim 10^{-5} \text{Mpc}^{-3}$ roughly following the baryon density and immersed in fields up to a few micro Gauss, whereas the observer is surrounded by fields $\ll 10^{-7} \text{G}$. In addition, we note that *if* the sources are homogeneously distributed, the best fit density of the three values considered in Tab. I (scenarios 5, 7, and 8) turns out to be the intermediate one, $n_s \sim 2.4 \times 10^{-5}$, in rough agreement with Ref. [19]. However, the likelihood is a very shallow function of n_s and implies uncertainties of at least an order of magnitude.

To illustrate the general impact of an EGMF on propagation, we show in Fig. 5 the distributions of delay times τ with respect to straight line propagation with arrival energies E , averaged over all realizations for scenario 6 in Tab. I. Note that the various peaks at small time delays $\tau \lesssim 10^4$ yr are due to UHECRs from discrete, nearby sources which mostly see the relatively weak fields around Earth in this scenario. One can show that the number

TABLE I: List of simulated scenarios. The columns contain the number assigned to the scenario, the source density, whether the sources are distributed as the baryon density in the large scale structure simulation box or homogeneously (yes/no), the observer position 1 or 2 corresponding to Fig. 3 and 4, respectively, the magnetic field strength at the observer location (zero indicates no fields, whereas a number indicates the EGMF obtained from the large scale structure simulation), the best fit power law index in the injection spectrum $E^{-\alpha}$, and the overall likelihoods of fits to the data. The first six likelihoods are for the multi-poles Eq. (3) above the energy indicated as superscript in EeV and over the range of l indicated as subscript. “AGASA only” and “AGASA+SUGAR” indicates which exposure functions and data sets were used. Above 40 EeV this corresponds to $N_{\text{obs}} = 99$ “AGASA+SUGAR” events, or to $N_{\text{obs}} = 57$ “AGASA only” events. Above 10 EeV comparison with an isotropic distribution of 1500 events was made, see text for more details. The last two likelihoods are for the auto-correlation Eq. (4) for $\theta \leq 20^\circ$, and the clustering within 2.5° up to multiplicity 10, respectively. The likelihoods are computed for $n = 4$ in Eq. (5) which leads to reasonable discriminative power.

#	n_s [Mpc $^{-3}$]	structure	observer	B_{obs}/G	α	$\mathcal{L}_{l \leq 10}^{40}$ AGASA only	$\mathcal{L}_{l=1}^{40}$	$\mathcal{L}_{l \leq 10}^{40}$	$\mathcal{L}_{l=1}^{40}$	$\mathcal{L}_{l \leq 10}^{10}$	$\mathcal{L}_{l=1}^{10}$	$\mathcal{L}_{\theta \leq 20^\circ}^{40}$	$\mathcal{L}_{n \leq 10}^{40}$
1	2.4×10^{-4}	yes	1	1.3×10^{-7}	2.4	0.070	0.011	0.37	0.094	0.12	0.042	0.57	0.85
2	2.4×10^{-4}	yes	2	8.2×10^{-12}	2.4	0.43	0.35	0.52	0.48	0.16	0.18	0.52	0.85
3	2.4×10^{-4}	yes	1	0	2.6	0.23	0.15	0.37	0.39	0.15	0.15	0.42	0.73
4	2.4×10^{-5}	yes	1	0	2.6	0.25	0.21	0.33	0.48	0.11	0.19	0.30	0.65
5	2.4×10^{-5}	no	1	0	2.6	0.36	0.34	0.45	0.51	0.13	0.24	0.65	0.71
6	2.4×10^{-5}	yes	2	8.2×10^{-12}	2.4	0.49	0.32	0.79	0.62	0.17	0.24	0.56	0.83
7	2.4×10^{-4}	no	1	0	2.6	0.35	0.40	0.42	0.47	0.12	0.17	0.53	0.78
8	2.4×10^{-6}	no	1	0	3.0	0.36	0.45	0.19	0.51	0.10	0.17	0.24	0.48
9	2.4×10^{-4}	yes	2	0	2.6	0.32	0.31	0.51	0.49	0.13	0.20	0.50	0.75
10	2.4×10^{-5}	yes	2	0	2.6	0.24	0.70	0.32	0.46	0.10	0.18	0.46	0.65

of such peaks increases with the source density. For the same scenario 6, Fig. 6 shows the distribution of UHECR deflection angles α with respect to the line of sight to the sources above various energy thresholds. This shows that deflection can be substantial even at the highest energies. Qualitatively this can be understood as follows: Neglecting energy loss processes, the r.m.s. deflection angle over a distance r in EGMF of r.m.s. strength B and coherence length l_c is $\theta(E, r) \simeq (2rl_c/9)^{1/2}/r_L$ [39], where the Larmor radius of a particle of charge Ze and energy E is $r_L \simeq E/(ZeB)$. In numbers this reads

$$\theta(E, r) \simeq 0.8^\circ Z \left(\frac{E}{10^{20} \text{ eV}} \right)^{-1} \left(\frac{r}{10 \text{ Mpc}} \right)^{1/2} \times \left(\frac{l_c}{1 \text{ Mpc}} \right)^{1/2} \left(\frac{B}{10^{-9} \text{ G}} \right), \quad (6)$$

for $r \gtrsim l_c$. Keeping in mind that sources are correlated with relatively strong fields and that according to Fig. 2 $\simeq 10\%$ of the volume is filled with fields $\gtrsim 10 \text{ nG}$, we can see that deflections of order 20 degrees up to 10^{20} eV should therefore not be surprising. It is interesting to note in this context that, as can be seen from Figs. 2-4, the EGMF in our simulations tend to be more extended than the baryons and thus the distribution of sources if they follow the baryons. A significant part of the total deflection can therefore be contributed by fields that are not in the immediate environment of the sources. Furthermore, for the source density $n_s \simeq 2.4 \times 10^{-5} \text{ Mpc}^{-3}$ of the typical scenario 6 of Tab. I, the average distance to the closest source is $\simeq 15 \text{ Mpc}$, and thus close enough to make magnetized regions of several Mpc around the

sources extend of order ten degrees on the sky, see also Fig. 4, upper panel.

The analytical approximation for the time delay corresponding to the deflection Eq. (6) is $\tau(E, r) \simeq r\theta(E, r)^2/4$, or

$$\tau(E, r) \simeq 1.5 \times 10^3 Z^2 \left(\frac{E}{10^{20} \text{ eV}} \right)^{-2} \left(\frac{r}{10 \text{ Mpc}} \right)^2 \times \left(\frac{l_c}{\text{Mpc}} \right) \left(\frac{B}{10^{-9} \text{ G}} \right)^2 \text{ yr}. \quad (7)$$

These numbers are consistent with Fig. 5 if one takes into account that the typical propagation distance drops from a few hundred Mpc at $\sim 10^{19} \text{ eV}$ to $\lesssim 30 \text{ Mpc}$ above $\simeq 10^{20} \text{ eV}$. Finally, Fig. 7 shows, for this same scenario, the predicted structure of arrival direction distributions.

Sufficient data to definitely discriminate among the different scenarios presented in Tab. I, e.g. the presence of diffuse EGMF as well as UHECR source characteristics, will have to await the next-generation experimental facilities, such as the Pierre Auger [11] and EUSO [23] projects. To demonstrate what can be achieved with these new experiments, we will work out the predictions for various observable statistical quantities for UHECRs both above $4 \times 10^{19} \text{ eV}$ and 10^{20} eV for the Auger full sky observatory. For this we will assume an exposure about 25 times larger than AGASA, which is reachable after about three years of running experiment. It corresponds to ~ 1500 events observed above $4 \times 10^{19} \text{ eV}$ and ~ 30 events above 10^{20} eV if a GZK cutoff is present, or ~ 200 events above 10^{20} eV if no GZK cutoff is present. We will also sometimes consider ~ 5000 events above $4 \times 10^{19} \text{ eV}$,

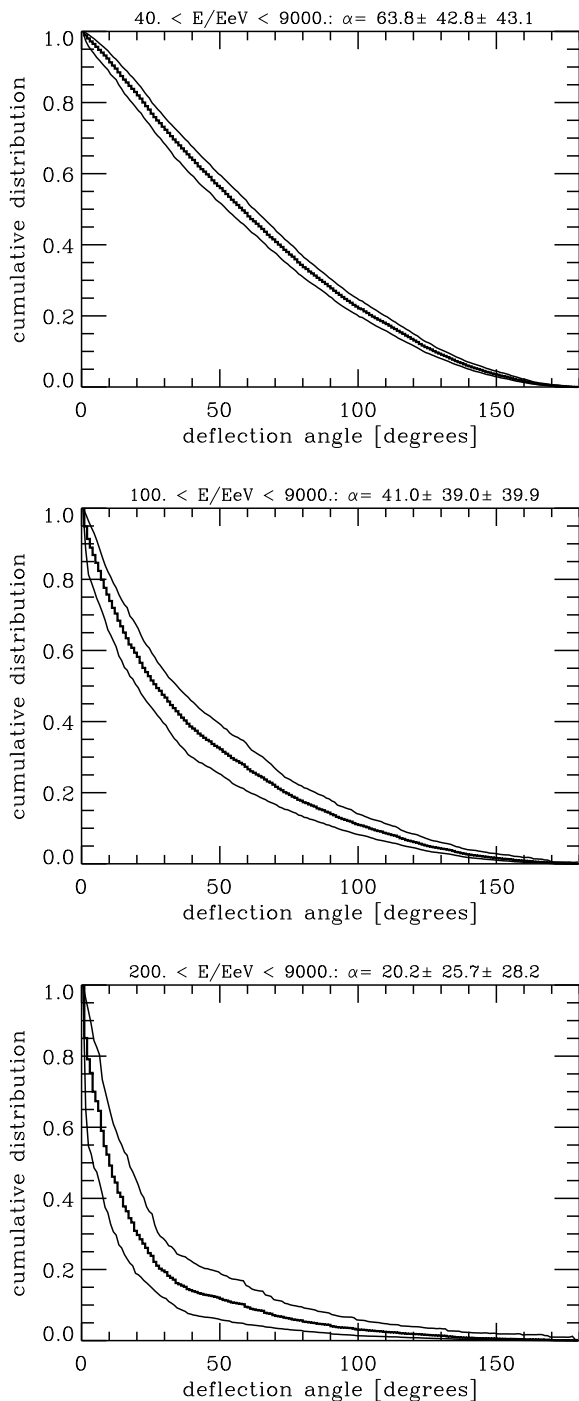


FIG. 6: The cumulative distribution of UHECR deflection angles with respect to the line of sight to the sources larger than α , averaged over 24 realizations for scenario 6 in Tab. I. Shown are the distributions (middle, histogram) and $1\text{-}\sigma$ variations (upper and lower curves) above 4×10^{19} eV (upper panel), above 10^{20} eV (middle panel), and above 2×10^{20} eV (lower panel). Also given on top of the figures average and variances of the distributions.

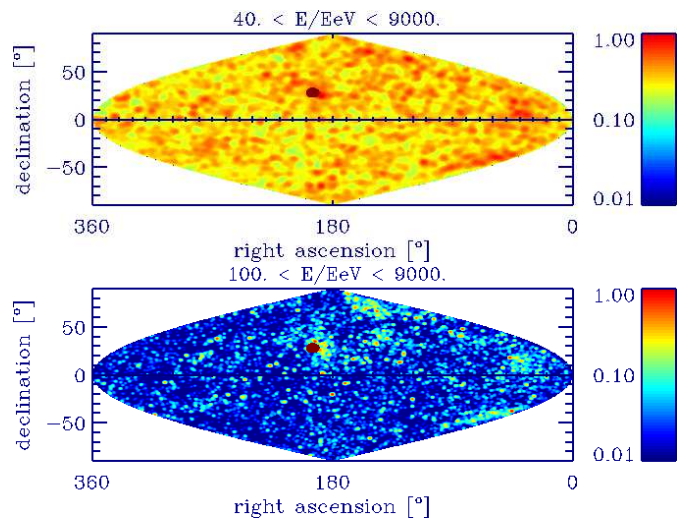


FIG. 7: Arrival direction distributions predicted within scenario 6 of Tab. I, averaged over 34 realizations of 10^4 simulated trajectories above 10^{19} eV each. The filled red sphere represents the overall direction to the supergalactic centre. Upper panel: $\approx 10^5$ events above 4×10^{19} eV, convoluted with an angular resolution of 2.5° . Lower panel: $\approx 10^4$ events above 10^{20} eV, convoluted with an angular resolution of 1° .

as is expected to be easily achieved by the EUSO experiment [23].

A. Signatures of structured versus homogeneous source distributions

One expects that the nonuniformity in the source distribution (*structure*) mostly influences the large scale multi-poles. Fig. 8 shows that, for a given source density, if magnetic deflection can be neglected, a homogeneous distribution of sources predicts, not surprisingly, an angular power spectrum more isotropic than a structured source distribution. Unfortunately, cosmic variance is sufficiently large that one can definitely discriminate the case of a structured distribution of sources only if the measured multi-poles happen to be several standard deviations above the prediction of a homogeneous distribution. This can happen only when the source luminosities are almost uniform, which is rather unrealistic. Otherwise, the measured multi-poles are consistent with both structured and unstructured source distributions, see Fig. 8. In addition, within cosmic variance, the multi-poles depend insignificantly on the source density. In contrast, magnetic fields tend to significantly decrease their values, while at the same time reducing cosmic variance, see Fig. 9. As a result, predictions of low-scale multi-poles above 4×10^{19} eV for next generation experiments tend to deviate from isotropy more significantly than for unmagnetized sources.

To demonstrate these tendencies more quantitatively, in Tab. II we provide the predictions for the sum of the

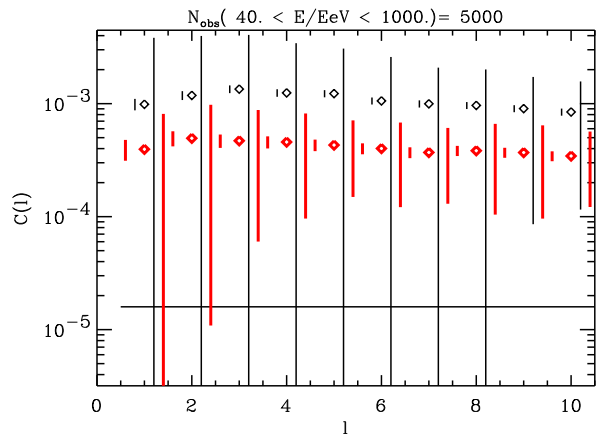
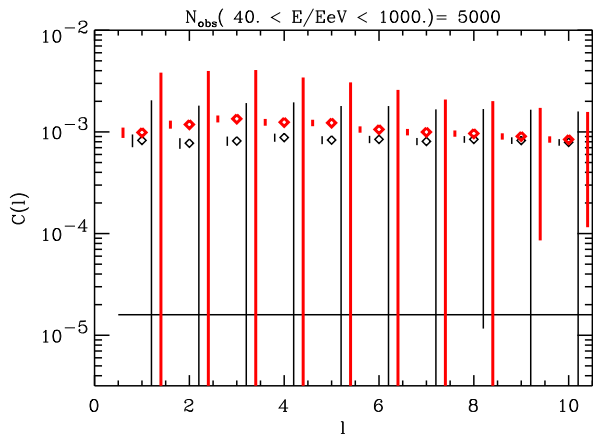
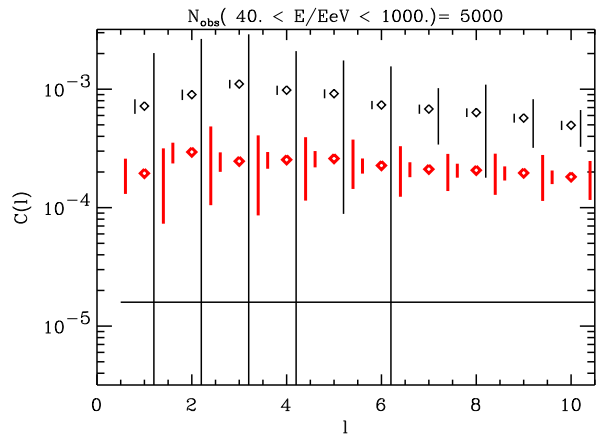
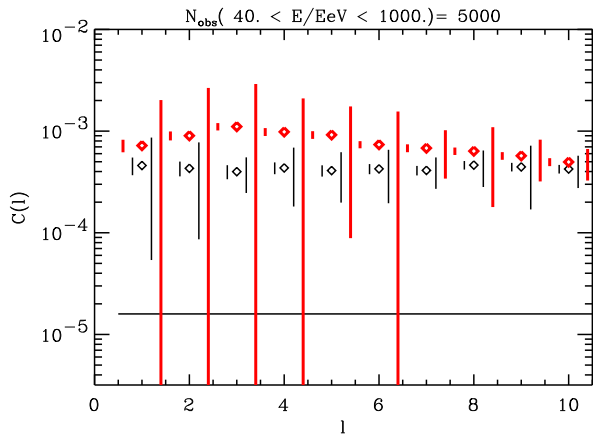


FIG. 8: Angular power spectrum $C(l)$ as a function of multi-pole l , for the full sky Pierre Auger observatory assuming $N_{\text{obs}} = 5000$ events observed above 4×10^{19} eV. The upper panel assumes sources with identical properties, whereas the luminosity function Eq. (1) was used in the lower panel. We show the realization averages (diamonds), statistical (left) and total (right) error bars, respectively, predicted by the model. The red (thick) diamonds and red (thick, outer) error bars represent scenario 4 (unmagnetized structured sources), whereas the black (thin) diamonds and black (thin, inner) error bars represent scenario 5 (unmagnetized homogeneously distributed sources). The source density is $n_s = 2.4 \times 10^{-5} \text{ Mpc}^{-3}$ in both cases. The straight line is the analytical prediction, $C_l \simeq (4\pi N_{\text{obs}})^{-1}$, for the average multi-poles for complete isotropy.

first ten multi-poles for the scenarios from Tab. I.

B. Source Density

If magnetic field effects can be neglected, the small-scale auto-correlation function will depend strongly on the source density: Few sources imply strong auto-correlations with considerable cosmic variance as well as strong clustering, whereas many sources imply weak

FIG. 9: Same as Fig. 8, but comparing predictions of structured sources with same densities and different magnetizations. The red (thick) diamonds and red (thick, outer) error bars represent scenario 6 (magnetized sources), whereas the black (thin) diamonds and black (thin, inner) error bars represent scenario 4 (unmagnetized sources).

auto-correlation with comparatively small cosmic variance. In the case of homogeneously distributed sources with identical properties this was indeed suggested as a measure of the source density [19]. Fig. 10 demonstrates that this is also true for structured sources. Furthermore, for a given source density the small scale auto-correlation is relatively insensitive to the structure of the source distribution, as becomes evident in Fig. 11.

However, if the sources are immersed in magnetic fields of order $\gtrsim 0.1 \mu\text{G}$, as they can occur in galaxy clusters and filaments, the auto-correlation function becomes almost insensitive to the source density and instead becomes a probe of source magnetization, as discussed below in Sect. 3.D. This is because a structured EGMF of such strength diffuses cosmic rays up to 10^{20} eV over the whole region immersed in such fields, as can be seen from the rough estimate Eq. (6). Therefore, the number of sources within such regions doesn't significantly affect

TABLE II: Predictions for the sum of the first ten multi-poles, $\sum_{l=1}^{10} C_l$, above 4×10^{19} eV for $N_{\text{obs}} = 5000$ observed events, with and without source luminosity variations according to Eq. (1). The two errors represent statistical and total (including cosmic variance) errors, as in the figures. The rows represent the scenarios of Tab. I.

	luminosity function Eq. (1), $10^3 \sum_{l=1}^{10} C_l$	constant luminosity, $10^3 \sum_{l=1}^{10} C_l$
2	$6.87 \pm 0.39 \pm 5.9$	$2.21 \pm 0.16 \pm 0.58$
3	$10.6 \pm 0.52 \pm 17$	$4.48 \pm 0.27 \pm 2.3$
4	$10.8 \pm 0.52 \pm 16$	$7.75 \pm 0.43 \pm 8.5$
5	$8.24 \pm 0.46 \pm 9.0$	$4.30 \pm 0.28 \pm 1.7$
6	$4.11 \pm 0.25 \pm 2.7$	$2.27 \pm 0.17 \pm 0.69$
7	$8.30 \pm 0.46 \pm 9.4$	$2.57 \pm 0.18 \pm 0.55$
8	$14.8 \pm 0.75 \pm 16$	$14.9 \pm 0.73 \pm 16$
9	$9.07 \pm 0.49 \pm 13$	$2.88 \pm 0.20 \pm 0.57$
10	$11.4 \pm 0.58 \pm 12$	$8.38 \pm 0.48 \pm 5.1$

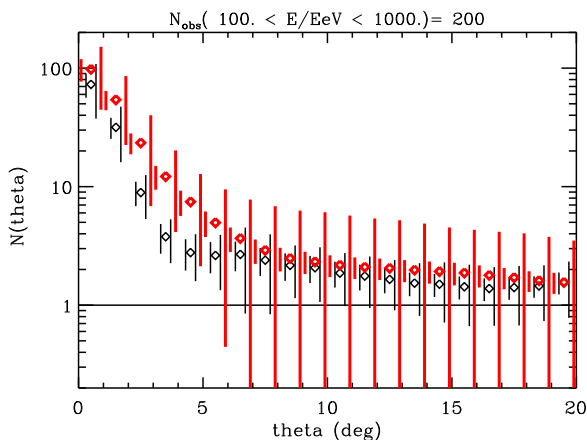


FIG. 10: The auto-correlation function for $N_{\text{obs}} = 200$ events observed above 10^{20} eV for the full sky Pierre Auger observatory for a bin size of $\Delta\theta = 1^\circ$. Averages and errors are as in Fig. 8. Compared are unmagnetized structured sources with different densities: The red (thick) diamonds and red (thick, outer) error bars represent scenario 4 ($n_s = 2.4 \times 10^{-5} \text{Mpc}^{-3}$), whereas the black (thin) diamonds and black (thin, inner) error bars represent scenario 3 ($n_s = 2.4 \times 10^{-4} \text{Mpc}^{-3}$) in Tab. I.

the auto-correlations any more, which increases the uncertainty in the source density.

C. Source Luminosity Function

If the source luminosity function is parametrized by $dn_s/dQ \propto Q^{-\alpha}$ in an interval $Q_{\text{min}} \leq Q \leq Q_{\text{max}}$, then for $\alpha \ll 2$ the most luminous sources will dominate, whereas for $\alpha \gg 2$ the weakest sources will dominate. These two cases will therefore be approximated by scenarios with sources of identical properties and cosmic variance is expected to be minimal. In contrast, $\alpha \simeq 2$ implies that all

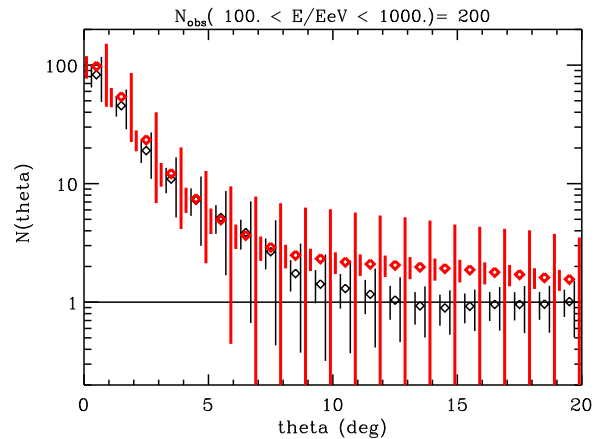


FIG. 11: Same as Fig. 10, but comparing unmagnetized sources with the same density $n_s = 2.4 \times 10^{-5} \text{Mpc}^{-3}$ with structured and unstructured distributions: The red (thick) diamonds and red (thick, outer) error bars represent scenario 4 (structured source distribution), whereas the black (thin) diamonds and black (thin, inner) error bars represent scenario 5 (homogeneous source distribution) in Tab. I.

luminosities contribute approximately equally to the observed flux. This is close to the case we chose in Eq. (1) which therefore tends to maximize cosmic variance. As can be seen from Fig. 12, in this case the uncertainties of large scale multi-poles due to cosmic variance are in general larger than the ones due to the finite number of events observed, even for the relatively sparse data set currently available. For the small scale properties described by the auto-correlation function and cluster frequencies, for $N_{\text{obs}} \lesssim 100$, cosmic variance is in general smaller than or comparable to the statistical error, as can be seen from Figs. 10 and 11 and Figs. 13 and 14 below.

D. Source Magnetization

Scenarios 3 and 4 are somewhat disfavored by auto-correlation and clustering: Structured sources produce more clustering in the absence of magnetic fields, as can be seen, for example, in Fig. 13. While this effect is marginal in the current data set, it will develop into a strong discriminator for future experiments: Scenarios with no significant magnetic fields predict a stronger auto-correlation at small angles, independent of whether or not the sources are structured. This is because if sources are immersed in considerable magnetic fields, their images are smeared out, which also smears out the auto-correlation function over a few degrees.

As shown in Fig. 14, this effect is significant once $N_{\text{obs}} \gtrsim 10^3$ events are observed above 4×10^{19} eV, as will be the case for the Pierre Auger project, and also if $N_{\text{obs}} \gtrsim 100$ events are observed above 10^{20} eV, as could

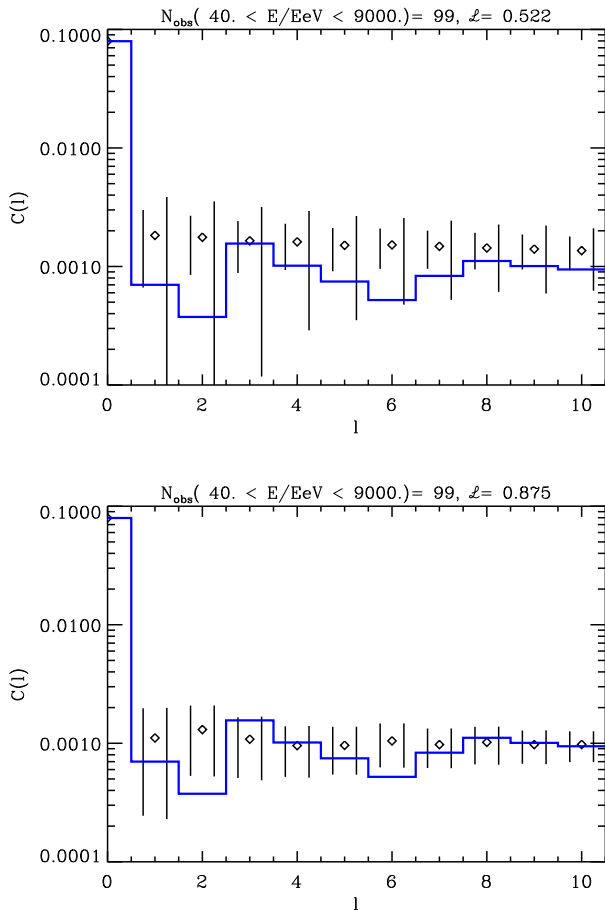


FIG. 12: The angular power spectrum $C(l)$ as a function of multi-pole l , predicted for the AGASA+SUGAR exposure function (see text), for $N_{\text{obs}} = 99$ events observed above 40 EeV, sampled from the simulated configurations of scenario 2 in Tab. I. The diamonds indicate the realization averages, and the left and right error bars represent the statistical and total (including cosmic variance due to different realizations) error, respectively, see text for explanations. The histogram represents the AGASA+SUGAR data. The overall likelihood significance for $n = 4$ and $l \leq 10$ in Eq. (5) appears at the top of the figures. The upper panel takes into account cosmic variance due to variation of source properties assumed to be parameterized by Eq. (1). The lower panel assumes that all sources have identical properties and thus cosmic variance is uniquely due to variation in source location.

be achieved, for example, by the EUSO project. At these energies the strongest auto-correlation at small angles is predicted by scenario 4 in Tab. I, where sources follow the large scale structure in the absence of magnetic fields. For a given source density, the auto-correlation predicted by homogeneously distributed sources in the absence of magnetic fields (scenario 5 in Tab. I) lies in between the one predicted by structured sources in the absence of magnetic fields (scenario 4 in Tab. I) and the one of structured sources with magnetic fields (scenario

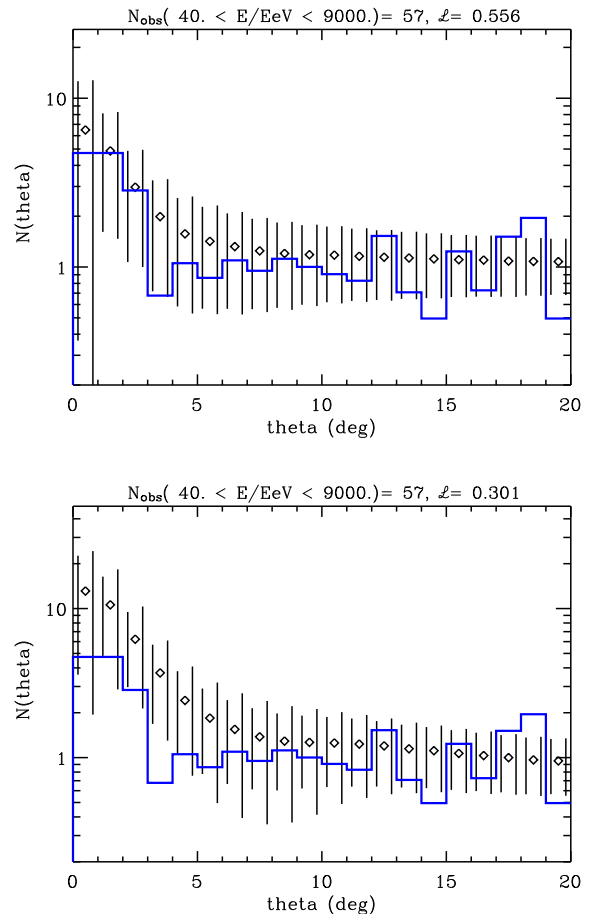


FIG. 13: The angular correlation function $N(\theta)$ as a function of angular distance θ , predicted for a bin size of $\Delta\theta = 1^\circ$ for the AGASA exposure function (see text), for $N_{\text{obs}} = 57$ events observed above 40 EeV, sampled from the simulated configurations. Note that an isotropic distribution would correspond to $N(\theta) = 1$. Averages and errors are as in Fig. 8. The histogram represents the AGASA data. The two scenarios shown correspond to structured sources of equal density with (scenario 6, upper panel) and without (scenario 4, lower panel) magnetization. The overall likelihood significance for $n = 4$ and $\theta \leq 10^\circ$ in Eq. (5) appears at the top of the figures. It is not significantly different for somewhat larger bin sizes $\Delta\theta \simeq 2^\circ$.

6 in Tab. I).

As an example, the predictions for the auto-correlation function in the first degree bin are summarized in Tab. III. This also confirms the discussion in Sect. 3.B: For structured sources in the absence of magnetic fields, the degree-scale auto-correlation function decreases with increasing source density, whereas it is rather independent of the source density if the sources are immersed in magnetic fields. Finally we observe that the low- l auto-correlation in case of magnetized sources hardly depends on their densities, as can be seen by comparing scenarios 2 and 6 in Tab. III. In contrast, for unmagnetized

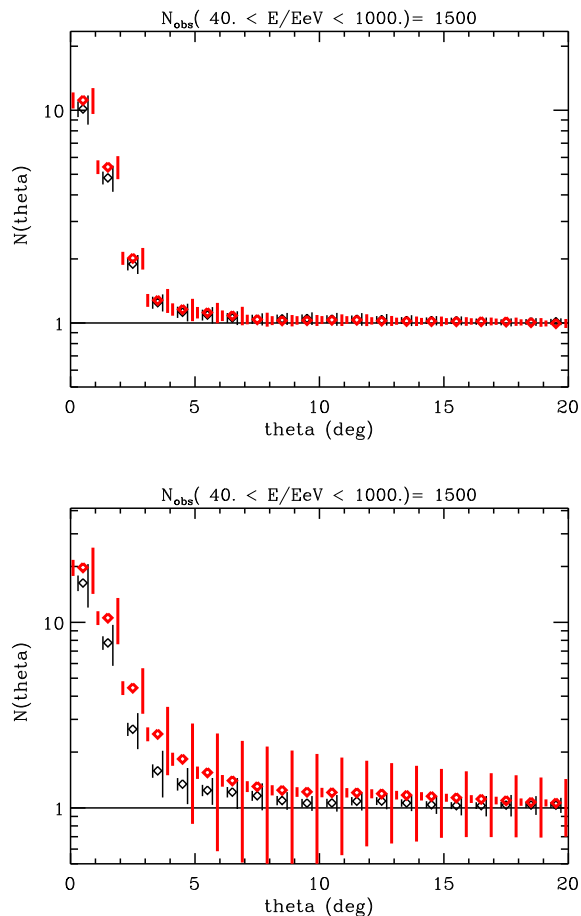


FIG. 14: The auto-correlation function for $N_{\text{obs}} = 1500$ events observed above 40 EeV for the full sky Pierre Auger observatory. Upper panel: Comparing magnetized sources with different densities. The red (thick) diamonds and red (thick, outer) error bars represent scenario 6 ($n_s = 2.4 \times 10^{-5} \text{ Mpc}^{-3}$), whereas the black (thin) diamonds and black (thin, inner) error bars represent scenario 2 ($n_s = 2.4 \times 10^{-4} \text{ Mpc}^{-3}$) in Tab. I. Lower panel: Same as upper panel, but in the absence of magnetic fields, i.e. comparing scenario 4 (red, thick set) with scenario 3 (black, thin set) in Tab. I.

sources the degree-scale auto-correlation is quite sensitive to the source density and always significantly higher than for magnetized discrete sources. This is clearly demonstrated by Fig. 14. A consequence of this is that in the absence of magnetic fields the auto-correlation function and its fluctuations can indeed be used as a measure of the source density, as suggested in Ref. [19]: The strength of the auto-correlation at small scales as well as its cosmic variance at all scales increase with decreasing source density. However, this effect can be almost completely erased by magnetic fields surrounding the sources. Such fields also tend to considerably reduce the effects of cosmic variance, especially at low source densities, as Fig. 14 demonstrates. This is also reflected by the fact that oscillations predicted to occur in the actually measured

TABLE III: Predictions for the auto-correlation function in the first degree bin, $N(1^\circ)$, for various threshold energies and number of observed events N_{obs} . The two errors represent statistical and total (including cosmic variance) errors, as in the figures. The rows represent the scenarios of Tab. I.

#	$E \geq 10^{20} \text{ eV},$ $N_{\text{obs}} = 200$	$E \geq 4 \times 10^{19} \text{ eV},$ $N_{\text{obs}} = 1500$
2	$45.4 \pm 12 \pm 17$	$10.1 \pm 0.86 \pm 1.6$
3	$72.9 \pm 17 \pm 35$	$16.3 \pm 1.6 \pm 4.3$
4	$98.0 \pm 21 \pm 53$	$19.7 \pm 2.0 \pm 5.5$
5	$83.0 \pm 18 \pm 34$	$15.9 \pm 1.5 \pm 3.4$
6	$44.8 \pm 12 \pm 19$	$11.2 \pm 0.97 \pm 1.6$
7	$60.8 \pm 15 \pm 30$	$13.1 \pm 1.3 \pm 2.2$
8	$191 \pm 33 \pm 88$	$37.9 \pm 3.1 \pm 11.6$
9	$68.6 \pm 17 \pm 37$	$14.4 \pm 1.4 \pm 3.6$
10	$100 \pm 21 \pm 40$	$20.2 \pm 1.9 \pm 4.4$

auto-correlation function, i.e. predicted for a given realization of sources and magnetic fields, are considerably suppressed by magnetic fields. This is demonstrated by Fig. 15.

Furthermore, Tab. III shows that the small-scale auto-correlation is rather independent of the observer position: The pairs of simulations 3, 9 and 4, 10 with unmagnetized sources differ only in the observer position, respectively, see Tab. I. Their predictions for the average degree-scale auto-correlations indeed differ by amounts much smaller than even the statistical error. This suggests that the concrete realization of the local large scale structure is mostly irrelevant to tendencies presented in the current paper.

As discussed in Sect. 3A, magnetized sources also tend to suppress large scale multi-poles as well as their cosmic variance. However, since unmagnetized sources, in particular in case of structured distributions, predict cosmic variances nearly as large as the averages of the multi-poles, small multi-poles cannot be used as a signature of strongly magnetized sources.

E. Magnetic Fields surrounding the Observer

If the observer is immersed in $\sim 0.1 \mu \text{ G}$ fields, considerable low- l multi-poles are predicted. This possibility is already disfavored by current data [22], as seen from Tab. I. We demonstrate this by comparing the predictions of scenarios with a strongly or negligibly magnetized observer for the large scale power spectrum above 10^{19} eV in Fig. 16. This can qualitatively be understood as follows [22]: The presence of a region with a relatively strong magnetic field surrounding the observer preferentially shields off UHECRs from sources that are farther away from the observer, in particular those outside of the magnetized region. In contrast, the flux from sources within the magnetized region is enhanced by the increased confinement time. Thus the observed flux is dominated by a few closer sources and appears more

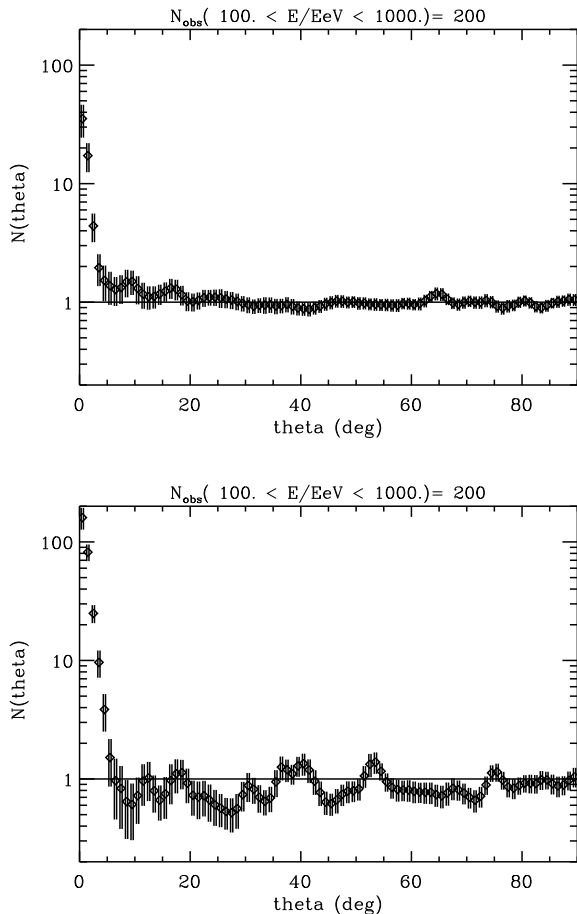


FIG. 15: The auto-correlation function for the full sky Pierre Auger observatory, for $N_{\text{obs}} = 200$ events observed above 100 EeV, predicted by one particular source realization for $n_s = 2.4 \times 10^{-5} \text{ Mpc}^{-3}$. Upper panel: scenario 6 in Tab. I, i.e. with magnetic fields. Lower panel: scenario 4 in Tab. I, i.e. without magnetic fields.

anisotropic.

Furthermore, scenarios in which the observer is immersed in an EGMF $\ll 0.1 \mu\text{G}$ predict UHECR spectra with a pronounced GZK cutoff. In contrast, if the observer is strongly magnetized the cutoff is attenuated. One can understand this as a partial compensation between energy attenuation lengths which decrease with increasing energy and magnetic diffusion lengths which increase with energy. As long as the source density is sufficiently high around the observer, the number of sources contributing to the flux decreases more slowly with increasing energy than in the absence of magnetic fields. For a strongly magnetized observer the observed spectrum appears to be less modified with respect to the injection spectrum. This tendency is confirmed by our Monte Carlo simulations, see Fig. 17.

By comparing auto-correlations and clustering in scenarios with and without EGMF we also confirmed that magnetic lensing [40] is insignificant for these highly

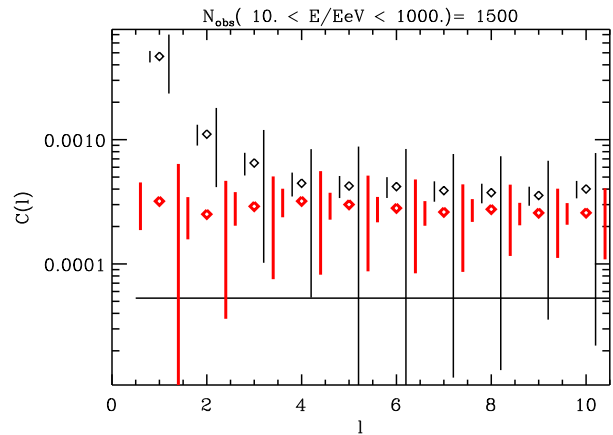


FIG. 16: The angular power spectrum obtained for the combined AGASA+SUGAR exposure function, for $N_{\text{obs}} = 1500$ events observed above 10 EeV. The red (thick) diamonds and red (thick, outer) error bars represent scenario 6, whereas the black (thin) diamonds and black (thin, inner) error bars represent scenario 1. The line key is as in Fig. 8.

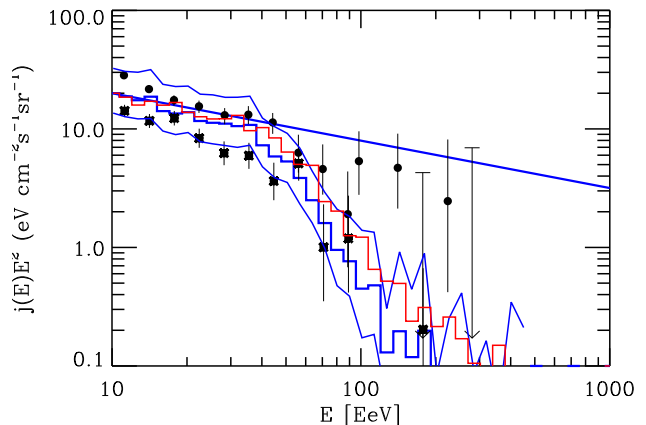


FIG. 17: Predicted spectrum observable by AGASA for scenario 2 (weakly magnetized observer), as compared to the AGASA (dots) and HiRes-I [9] (stars) data. The histogram marks the average and the two lines above and below the 1-sigma fluctuations over the simulated realizations. The solid straight line marks the injection spectrum. For comparison shown (red, thin histogram) is the spectrum predicted by scenario 1 (strongly magnetized observer). Both cases correspond to the same source density $n_s = 2.4 \times 10^{-4} \text{ Mpc}^{-3}$.

structured EGMF, even for cases where the observer is immersed in strong magnetic fields.

IV. DISCUSSION AND CONCLUSIONS

We studied the effects of non uniform UHECR source distributions and EGMF imprinted in the multi-pole mo-

ments, auto-correlation function, and cluster statistics of UHECRs with energies above 10^{19} eV. We compared scenarios where the sources are distributed homogeneously or according to the baryon density distribution obtained from a simulation of the large scale structure of the Universe. We also compared the case in which the sources are all identical and in which their power and spectra of injected UHECRs are distributed according to functions that maximize cosmic variance. The changes in the results due to variation in the locations and properties of the sources were evaluated as cosmic variance. The source luminosity function was chosen close to the critical case where all luminosities contribute comparably to the observed flux in a logarithmic distribution, which tends to maximize cosmic variance. In this case we found that cosmic variance of large scale multi-poles tends to be larger than the statistical fluctuations if the number of observed events is $\gtrsim 100$. In all other cases, notably for the auto-correlations and cluster multiplicities, cosmic variance is small compared to statistical fluctuations for $N_{\text{obs}} \lesssim 100$ events.

The influence of EGMF is assessed by comparing the case of UHECR propagation when (a) EGMF are negligible and (b) they are not and are modeled through a simulation of large scale structure formation and magnetic field evolution. In the latter case the magnetic fields were normalized so as to reproduce published values of Faraday rotation measures for clusters of galaxies and filaments [26, 29]. We chose two cases for the location of the observer: in a relatively high field region with $B \simeq 0.1 \mu\text{G}$ and in a negligible field region with $B \simeq 10^{-11}$ G.

In Ref. [3] it was found that in the case of structured magnetic fields an observer immersed in $\sim 0.1 \mu\text{G}$ fields was marginally favored whereas isotropy observed at 10^{19} eV could not be explained by the local component alone. In Ref. [22] and in the present paper we took into account the contribution of sources beyond the large scale structure simulation box by making use of the periodic boundary conditions of the simulation box. As a result we found that the AGASA data is consistent with and even marginally favors scenarios with magnetic fields up to a few micro Gauss in galaxy clusters whose structure is obtained from the large scale structure simulation, and where the sources follow the baryon distribution. Contrary to Ref. [3] this scenario requires that the observer is in a relatively low field region, $B \ll 0.1 \mu\text{G}$. This also allows to explain isotropy observed at 10^{19} eV reasonably well. That the fit quality there is significantly worse than at higher energies, as can be seen from Tab. I, may have to do with significant evolution of the characteristics of sources at large distances whose contribution increases with decreasing UHECR energy. The best fit scenario also predicts a pronounced GZK cutoff as well as considerable deflection of order 20° up to $\simeq 10^{20}$ eV. *Thus, if this scenario is further confirmed by future experiments, charged particle astronomy may not be possible.*

Structured sources and magnetic fields up to a few micro Gauss in galaxy clusters and the Earth immersed

in relatively low EGMF $B \ll 0.1 \mu\text{G}$ in fact seem to be the most realistic scenario. Thus, already existing UHECR data allow probing the large scale structure distribution of UHECR sources and magnetic field! We have demonstrated how future detectors such as the Pierre Auger and EUSO projects can further probe EGMF and UHECR source characteristics: Strongly magnetized observers predict considerable large scale anisotropies between 10^{19} eV and 10^{20} eV which is already ruled out by current data on the percent level. Furthermore, strong fields surrounding the observer would predict a GZK cutoff that is less pronounced than for negligible fields. Low auto-correlations at degree scales imply magnetized sources quite independent of other source characteristics such as their density. The latter can only be estimated from the auto-correlations halfway reliably if magnetic fields have negligible impact on propagation. The multi-poles for $l \lesssim 10$ are relatively insensitive to the source density and on average tend to be smaller if sources are magnetized. At the same time, magnetized sources also tend to reduce cosmic variance of these multi-poles, and as a result their predictions above 4×10^{19} eV for future experiments tend to deviate from isotropy more significantly than for unmagnetized sources. Unfortunately, especially if source luminosities fluctuate considerably, it may be difficult to distinguish between structured and homogeneous source distributions even with next generation experiments.

For the required average local source number density and continuous power per source above 10^{19} eV we find $n_s \gtrsim 10^{-5} - 10^{-4} \text{Mpc}^{-3}$, and $Q_s \lesssim 10^{42} \text{erg s}^{-1}$ respectively, the latter within about one order of magnitude uncertainty to both sides. This corresponds to an average UHECR emissivity of $q_{\text{UHECR}} = n_s Q_s \sim 1.5 \times 10^{37} \text{erg Mpc}^{-3} \text{s}^{-1}$, with an uncertainty likely somewhat smaller than for the above quantities, since it is fixed by the observed UHECR flux. Note that the uncertainty in n_s is increased by the structured EGMF which tends to mix contributions from individual sources residing in these fields.

A simple study of deflection angles in the context of a constrained large scale structure simulation has recently been undertaken in Ref. [17]. They find maximal deflection angles of a few degrees above 4×10^{19} eV, considerably smaller than in our present study. This may be due to at least two reasons: First, these authors do not study structured sources which tend to be in regions of high density and magnetic fields which introduces a bias towards small deflection in the case of Ref. [17]. In fact, if we take the EGMF scenario corresponding to scenario 2 in Tab. I, but with a homogeneous source distribution instead, we obtain average deflection angles of $\simeq 61^\circ$ above 4×10^{19} eV, $\simeq 33^\circ$ above 10^{20} eV, and $\simeq 10^\circ$ above 2×10^{20} eV. This is smaller than the deflection angles obtained in scenarios where source positions and strong magnetic fields are correlated, see Fig. 6, but still considerably larger than values obtained in Ref. [17]. In fact, even if the magnetic field strength is reduced by a factor

10 in our simulations, the average deflection angle above 4×10^{19} eV is still $\sim 30^\circ$, only a factor $\simeq 2.2$ smaller. This non-linear behavior of deflection with field normalization is mostly due to the strongly non-homogeneous character of the EGMF. Note that a field strength normalization reduction by a factor 10 corresponds to a left-shift of the x-axis in Fig. 1 of two decades, such that the EGMF is virtually dynamically unimportant in all cells of the simulation.

The remaining discrepancy in typical UHECR deflection between our present work and Ref. [17], for cases meaningful to compare, is most likely due to the different EGMF models used by the different authors. A detailed consideration of these differences is well beyond the scope of this paper, although we plan to investigate this issue further in a forthcoming paper. So little is known about large scale magnetic fields and their evolu-

tion. This makes signatures for magnetized sources, as discussed in the present paper, even more important.

Acknowledgments

We would like to thank Martin Lemoine and Claudia Isola for earlier collaborations on the codes partly used in this work. The work by FM was partially supported by the Research and Training Network ‘‘The Physics of the Intergalactic Medium’’ set up by the European Community under the contract HPRN-CT2000-00126 RG29185. GS thanks the Max-Planck-Institut für Physik, Werner Heisenberg Institut where part of this work has been performed for hospitality and financial support.

-
- [1] for recent reviews see J. W. Cronin, *Rev. Mod. Phys.* 71 (1999) S165; M. Nagano, A. A. Watson, *Rev. Mod. Phys.* 72 (2000) 689; A. V. Olinto, *Phys. Rept.* 333-334 (2000) 329; X. Bertou, M. Boratav, and A. Letessier-Selvon, *Int. J. Mod. Phys. A* 15 (2000) 2181; G. Sigl, *Science* 291 (2001) 73; F. Stecker, *J. Phys. G.* 29 (2003) R47.
- [2] ‘‘Physics and Astrophysics of Ultra High Energy Cosmic Rays’’, *Lecture Notes in Physics*, vol. 576 (Springer Verlag, 2001), eds. M. Lemoine, G. Sigl.
- [3] G. Sigl, F. Miniati, and T. Enßlin, *Phys. Rev. D* 68 (2003) 043002.
- [4] W. S. Burgett and M. R. O’Malley, *Phys. Rev. D* 67 (2003) 092002.
- [5] Y. Uchihori, M. Nagano, M. Takeda, M. Teshima, J. Lloyd-Evans, and A. A. Watson, *Astropart. Phys.* 13 (2000) 151.
- [6] K. Greisen, *Phys. Rev. Lett.* 16 (1966) 748; G. T. Zatsepin and V. A. Kuzmin, *Pis’ma Zh. Eksp. Teor. Fiz.* 4 (1966) 114 [*JETP. Lett.* 4 (1966) 78].
- [7] F. W. Stecker, *Phys. Rev. Lett.* 21 (1968) 1016.
- [8] D. R. Bergman, *Nucl. Phys. B, Proc. Suppl.* 117 (2003) 106; *Proc. 28th International Cosmic Ray Conference, Tsukuba*, vo. 1, p. 397 (2003), see <http://www-rccn.icrr.u-tokyo.ac.jp/icrc2003/PROCEEDINGS/PDF/BOOK.pdf>.
- [9] R. U. Abasi et al. (HiRes collaboration), *Phys. Rev. Lett.* 92 (2004) 151101; e-print astro-ph/0208301.
- [10] M. Takeda et al., *Phys. Rev. Lett.* 81 (1998) 1163; *Astrophys. J.* 522 (1999) 225; Hayashida et al., e-print astro-ph/0008102; see also <http://www-akeno.icrr.u-tokyo.ac.jp/AGASA/>.
- [11] J. W. Cronin, *Nucl. Phys. B (Proc. Suppl.)* 28B (1992) 213; *The Pierre Auger Observatory Design Report* (ed. 2), March 1997; see also <http://www.auger.org>.
- [12] G. Sigl, M. Lemoine, and P. Biermann, *Astropart. Phys.* 10 (1999) 141.
- [13] C. Isola, M. Lemoine, and G. Sigl, *Phys. Rev. D* 65 (2002) 023004.
- [14] M. Lemoine, G. Sigl, and P. Biermann, e-print astro-ph/9903124.
- [15] T. Stanev, e-print astro-ph/0303123; T. Stanev, D. Seckel, and R. Engel, *Phys. Rev. D* 68 (2003) 103004; see also T. Stanev, R. Engel, A. Mücke, R. J. Protheroe, and J. P. Rachen, *Phys. Rev. D* 62 (2000) 093005.
- [16] C. Isola and G. Sigl, *Phys. Rev. D* 66 (2002) 083002.
- [17] K. Dolag, D. Grasso, V. Springel, and I. Tkachev, e-print astro-ph/0310902.
- [18] P. Sommers, *Astropart. Phys.* 14 (2001) 271.
- [19] P. Blasi and D. De Marco, *Astropart. Phys.* 20 (2004) 559.
- [20] H. Yoshiguchi, S. Nagataki, S. Tsubaki, and K. Sato, *Astrophys. J.* 586 (2003) 1211; H. Yoshiguchi, S. Nagataki, and K. Sato, *Astrophys. J.* 592 (2003) 311; *Astrophys. J.* 596 (2003) 1044.
- [21] G. Medina Tanco, ‘‘Cosmic magnetic fields from the perspective of ultra-high-energy cosmic rays propagation’’, *Lect. Notes Phys.* 576 (2001) 155.
- [22] G. Sigl, F. Miniati, and T. Enßlin, e-print astro-ph/0309695.
- [23] See <http://www.euso-mission.org>.
- [24] G. Medina-Tanco, E. M. De Gouveia Dal Pino, and J. E. Horvath, e-print astro-ph/9707041.
- [25] F. Miniati, *Mon. Not. R. Astron. Soc.* 337 (2002) 199.
- [26] D. Ryu, H. Kang, and P. L. Biermann, *Astron. Astrophys.* 335 (1998) 19.
- [27] R. O. Kulsrud, R. Cen, J. P. Ostriker, and D. Ryu, *Astrophys. J.*, 480 (1997) 481.
- [28] P. P. Kronberg, H. Lesch, and H. Ulrich, *Astrophys. J.* 511 (1999) 56.
- [29] P. P. Kronberg, *Reports of Progress in Physics* 58 (1994) 325; J. P. Vallée, *Fundamentals of Cosmic Physics*, Vol. 19 (1997) 1; T. E. Clarke, P. P. Kronberg, and H. Böhringer, *Astrophys. J. Lett.* 547 (2001) L111; J.-L. Han and R. Wielebinski, *Chinese Journal of Astronomy and Astrophysics* 2 (2002) 293 [e-print astro-ph/0209090]; P. P. Kronberg, *Physics Today* 55, December 2002, p. 40.
- [30] F. Miniati, Ph.D. Thesis, University of Minnesota 2000; F. Miniati, T. W. Jones, H. Kang, and D. Ryu, *Astrophys. J.* 562 (2001) 233.
- [31] R. Fusco-Femiano, D. Dal Fiume, L. Feretti, G. Giovannini, P. Grandi, G. Matt, S. Molendi, A. Santangelo, 513 (1999) L21.

- [32] J. Bagchi, T. A. Ensslin, F. Miniati, C.S. Stalin, M. Singh, S. Raychaudhury, N.B. Humeshkar, *New Astronomy*, 7 (2002) 249.
- [33] J. Chiang and R. Mukherjee, *Astrophys. J.* 496 (1998) 752.
- [34] P. Bhattacharjee and G. Sigl, *Phys. Rept.* 327 (2000) 109; L. Anchordoqui, T. Paul, S. Reucroft, and J. Swain, *Int. J. Mod. Phys. A* 18 (2003) 2229.
- [35] R. G. Brownlee et al., *Can. J. Phys.* 46 (1968) S259; M. M. Winn et al., *J. Phys. G* 12 (1986) 653; R. W. Clay et al., *Astron. Astrophys.* 255 (1992) 167; L. J. Kewley, R. W. Clay, and B. R. Dawson, *Astropart. Phys.* 5 (1996) 69; C. J. Bell et al., *J. Phys. A* 7 (1974) 990; see also <http://www.physics.usyd.edu.au/hienergy/sugar.html>.
- [36] M. Kachelrieß and D. V. Semikoz, *Phys. Lett. B* 577 (2003) 1; H. B. Kim and P. Tinyakov, e-print astro-ph/0306413.
- [37] B. T. Stokes, C. C. H. Jui, and J. N. Matthews, *Astropart. Phys.* 21 (2004) 95.
- [38] L. Anchordoqui et al., *Phys. Rev. D* 68 (2003) 083004.
- [39] E. Waxman and J. Miralda-Escudé: *Astrophys. J.* 472 (1996) L89.
- [40] see, e.g., D. Harari, S. Mollerach, E. Roulet, F. Sanchez, *JHEP* 0203 (2002) 045.